2026 IEEE International Conference on Robotics and Automation (ICRA 2026)
June 1-5, 2026. Vienna, Austria

Unified Magnetic 5-DoF Localization Framework for Capsule Robots via PMMN-DBO: From Single- to Multi-Robot Scenarios with Real-Time Control–Localization Co-Design

Zijin Zeng[1], Chan Li[1], Zaiyang Chen[1], Shunxiao Huang[1], Wenyan Niu[1], Hongyan Sun[1], Menglu Tan[2,†], Yingjian Guo[1,†], and Lin Feng[1,3,†]

***Abstract*— Motivated by clinical needs for precise navigation and safety, low-latency and high-precision localization has become a key enabler for capsule robots. A unified magnetic 5-DoF high-precision localization framework for capsule robots is presented. Building on layered multi-source magnetic field modeling, online external-field compensation, and global optimization-based inversion, the framework achieves real-time decoupling between control and localization fields, while providing a unified interface compatible with diverse hardware configurations and operation modes. On this basis, the PMMN-DBO algorithm is proposed, delivering high-accuracy and efficient localization in single- and multi-capsule scenarios, and supports synchronized control–localization. Experimentally, for single-capsule localization, mean errors are 0.59 mm/0.69° with a 20.2 ms computation time, surpassing conventional methods. In multi-capsule settings, localization errors remain low with stable convergence: mean errors are 1.28 mm/1.13° for two capsules and 2.56 mm/2.83° for three capsules. Under synchronized control–localization, trajectory-tracking errors reach 1.33 mm/1.85°. Overall, the proposed framework is unified, high-precision, efficient, and flexible, laying a general and reusable foundation for clinical-grade precise navigation and closed-loop magnetic control.**

I. INTRODUCTION

Magnetically actuated capsule robots, envisioned as the next-generation platform for gastrointestinal diagnosis and therapy[1], [2], are transitioning from passive imaging to active perception and closed-loop manipulation[3]. In this context, precise, robust, and low-latency[4] pose estimation is fundamental for closed-loop control[5], accurate navigation, and safe interaction. Owing to the severe attenuation of electromagnetic waves in tissue, the open and unstructured clinical environment, and the limitations of vision/ultrasound under occlusion and heterogeneous media[6], magnetic localization has emerged as a broadly applicable solution: magnetic fields attenuate weakly in soft tissue, low-cost tri-axial magnetic sensors can be densely deployed, and magnetic localization naturally coexists with magnetic control systems[7]. However, deployment in real clinical scenarios still faces three major challenges.

1) Coupling and separation of multi-source magnetic fields: Clinical-grade magnetic control employs multiple coils or permanent magnets to generate time-varying control fields[8], which superimpose with the field of the capsule's internal magnet at the sensors and invalidate the assumption that "the measured field is solely determined by the capsule." It is therefore necessary to strip away the control field online without interrupting control, while suppressing static background and noise. 2) Cross-scale model unification is also required: the capsule's far field can be approximated as a dipole[9], whereas the coils exhibit complex near-field behavior at scales comparable to the workspace, for which analytic models often lack accuracy[10]; multiple field sources must be seamlessly fused under unified coordinates and interfaces to accommodate diverse hardware topologies and operation modes. 3) Real-time solution of high-dimensional, nonconvex, multimodal optimization: Pose estimation for a single capsule is nonconvex; multiple capsules increase dimensionality linearly and induce numerous local minima. Traditional linearization or strongly prior-driven filtering struggles to ensure convergence and global optimality under real-time constraints[11].

Existing methods—such as linear optimizers[12], nonlinear optimizers[13], particle swarm optimization (PSO)[14], Levenberg–Marquardt (LM)[15], LM–expec-tation maximization (LM–EM)[16], simulated annealing–PSO (SA–PSO)[17], and dung beetle optimizer (DBO)[18], [19]—perform well for single-capsule cases without control or with idealized coil geometries. Yet under complex near-field control and multi-capsule superposition, their performance is often degraded by model mismatch, inseparable fields, observability loss, and limited real-time capability[20].

To address these issues, this work proposes a unified 5-DoF magnetic localization framework that forms an end-to-end pipeline of layered multi-source field modeling, online external-field compensation, and global inversion. At the system level, a unified magnetic modeling and interface is adopted, fusing a dipole model for the capsule with near-field finite-element models for control coils; based on a 4×4 planar array of tri-axial magnetic sensors, online field separation decouples control and localization

*This work was supported by the National Key R&D Program of China (Grant No. 2022YFF1502000), Beijing Municipal Fund for Distinguished Young Scholars (Grant No. JQ22022), and Fundamental Research Funds for the Central Universities (Grant No. YWF-22-K-101).

[1]School of Mechanical Engineering & Automation, Beihang University, Beijing 100191, China.

[2]Academy of Artificial Intelligence, Beijing Institute of Petrochemical Technology, Beijing 102627, China.

[3]Beijing Advanced Innovation Center for Biomedical Engineering, Beijing 102433, China.

[†]Corresponding authors: Menglu Tan (e-mail: 2567834670@qq.com), Yingjian Guo (e-mail: yingjguo@126.com), and Lin Feng (e-mail: linfeng@buaa.edu.cn).

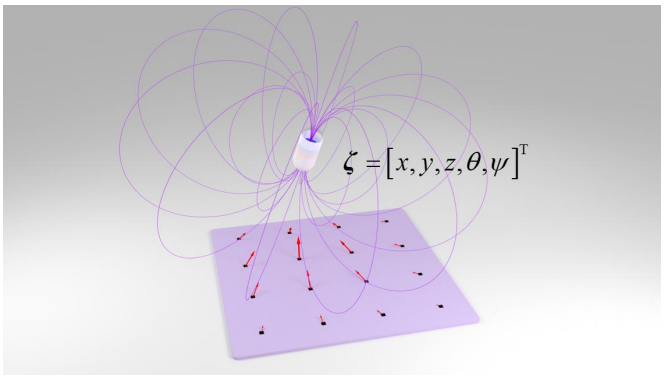

Fig. 1. Schematic of magnetic localization for capsule robots.

in real time. At the algorithmic level, an enhanced DBO variant, PMMN-DBO, is proposed. It incorporates parallel multi-task optimization, mirrored boundary reflection, elite-solution mutation, and a nonlinear convergence factor. These components improve global exploration and asymptotic convergence in high-dimensional, nonconvex, multimodal spaces. As a result, the method enables real-time, high-accuracy localization for single and multiple capsules under strong constraints. In terms of application, comprehensive validation is conducted across three core scenarios: precise single-capsule localization, coordinated multi-capsule localization, and synchronized control–localization. Results show that, compared with conventional optimizers, PMMN-DBO significantly improves accuracy while maintaining real-time performance, successfully achieving co-design of control and localization.

The remainder of the paper is organized as follows. Section II details the system architecture, layered modeling, and measurement separation, and formulates the problem as a constrained nonconvex optimization. Section III presents the PMMN-DBO mechanism and implementation. Section IV reports experiments and results for single/multi-capsule localization and synchronized control–localization. Section V concludes and discusses future work.

II. LOCALIZATION METHOD

A. System Architecture for Magnetic Localization

The capsule-robot magnetic localization system follows a general wireless localization paradigm based on magnetic field signatures: an external magnetic sensor array measures the composite magnetic field in real time within the workspace. Combined with layered modeling and an optimization solver, the system enables precise single-capsule localization, coordinated multi-capsule localization, and synchronized control–localization.

Principle of operation: a permanent magnet embedded in the capsule generates a characteristic magnetic field whose spatial distribution encodes the capsule's position and orientation. A distributed array of magnetic sensors measures the magnetic flux density vector at multiple locations. With appropriate magnetic field models, observation equations are constructed and an optimization routine solves for the pose parameters. Different magnetic sources are modeled accordingly: the capsule magnet is represented by a dipole model, while external control coils are described by a finite-element near-field model with interpolation. A unified magnetic-field computation interface and solver support single-agent localization, multi-agent cooperation, and control–localization synchronization. As schematized in Fig. 1, the system comprises three core modules: the capsule robot, the magnetic sensor array, and the signal-processing and localization engine. Define the effective workspace $V = \{(x, y, z) | 0 \le z \le h, (x, y) \in S\}$, where S denotes the horizontal projection area covered by the array.

B. Magnetic Field Fundamentals and Modeling

1) Capsule magnet modeling: The capsule integrates a cylindrically shaped permanent magnet whose magnetic moment aligns with the cylinder axis. For high-precision localization, a magnetic field model of the embedded magnet is established. The geometric center of the magnet is defined as the capsule position, and the magnetic moment direction as the capsule orientation. The 5-DoF pose is denoted by $\boldsymbol{\xi} = \left[x,\ y,\ z,\ \theta,\ \psi\right]^{\top} \in \mathbb{R}^5$, where the position is $\mathbf{p_m} = [x, y, z]^{\top} \in \mathbb{R}^3$, the elevation (pitch) angle is $\theta \in [0, \pi]$, and the azimuth (yaw) angle is $\psi \in [0, 2\pi)$. The roll angle is unobservable due to axial symmetry. The magnetic dipole moment is expressed as

$$\mathbf{m} = MV\hat{\mathbf{m}}(\theta, \psi), \tag{1}$$

where M is the magnetization, V is the magnet volume, and $\hat{\mathbf{m}}(\theta, \psi)$ is the unit vector along the dipole direction :

$$\hat{\mathbf{m}}(\theta, \psi) = [\sin\theta\cos\psi,\ \sin\theta\sin\psi,\ \cos\theta]^{\top}. \tag{2}$$

The dipole model is valid under a far-field condition $r \gg a$, where r is the distance from the sensor to the capsule and a is the characteristic magnet size (radius). In this work, the minimum detection distance is set to $r_{\min} = 5a$. When the capsule pose is $\boldsymbol{\xi}$, the magnetic flux density at the i-th sensor located at $\mathbf{p}_i$ is

$$\hat{\mathbf{B}}_i^{\text{cap}}(\boldsymbol{\xi}) = \frac{\mu_r \mu_0 MV}{4\pi|\mathbf{r}_i|^3}\left[3(\hat{\mathbf{m}}(\theta, \psi) \cdot \hat{\mathbf{r}}_i)\hat{\mathbf{r}}_i - \hat{\mathbf{m}}(\theta, \psi)\right]. \tag{3}$$

Here μ_r is the relative permeability of the magnet, $\mu_0 = 4\pi \times 10^{-7}$ H/m is the vacuum permeability, $\mathbf{r}_i = \mathbf{p}_i - \mathbf{p}_m, \hat{\mathbf{r}}_i = \mathbf{r}_i/|\mathbf{r}_i|$. This provides an analytical mapping from pose to magnetic flux density at arbitrary points, forming the basis for localization.

2) Control field modeling: To realize active functions such as rotation and propulsion, external coils generate time-varying control fields that impose forces and torques on the capsule. These fields superimpose on sensor measurements and must be removed online for accurate localization.

Because the control coils operate in a compact volume with coil size comparable to the workspace and complex geometries, far-field approximations and simple analytical models are insufficient. A finite element method (FEM) combined with 3D interpolation is therefore adopted to

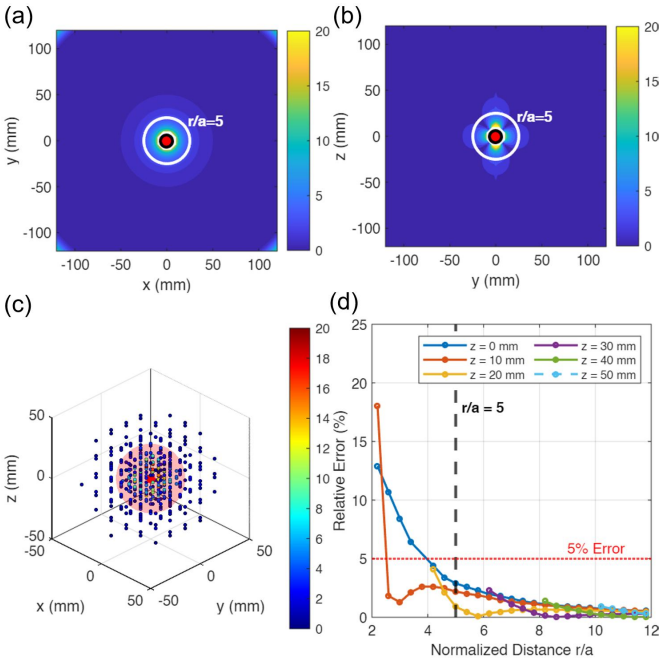

Fig. 2. Validation of dipole model validity and far-field threshold. (a) Relative magnetic field error on the x–y plane at $z = 0$. (b) Relative magnetic field error on the y–z plane at $x = 0$. (c) 3D error scatter distribution; the translucent red sphere indicates the theoretical far-field boundary $r/a = 5$. (d) Statistical curves of error versus distance across multiple z-planes.

model near fields. Assuming local linearity with respect to current within the coil workspace, a unit-current response is precomputed and stored for interpolation. For the j-th coil, define the unit-current response in its local frame C_j as

$$\mathbf{F}_j(\mathbf{q}) = \mathbf{B}_c(\mathbf{q}; I_j = 1A), \tag{4}$$

where $\mathbf{q}$ is a point in C_j. Let W be the world frame. The rigid transform from C_j to W is

$$\mathbf{T}_j = \begin{bmatrix} \mathbf{R}_j & \mathbf{t}_j \\ \mathbf{0} & 1 \end{bmatrix}, \tag{5}$$

with rotation $\mathbf{R}_j$ and translation $\mathbf{t}_j$ obtained via calibration and updated online. For the i-th sensor at world position $\mathbf{r}_i^s$, the magnetic field contributed by coil j is computed by "inverse transform to local – interpolate – rotate back to world – scale by current":

$$\mathbf{B}_{i,j}^{\text{coil}} = I_j \mathbf{R}_j \mathbf{F}_j(\mathbf{R}_j^\top(\mathbf{r}_i^s - \mathbf{t}_j)). \tag{6}$$

The total control field is the sum over all coils given their poses $(\mathbf{R}_j, \mathbf{t}_j)$ and currents I_j.

3) Multi-coil superposition: Under the quasi-static assumption and linear media, the net control field at sensor i from N_c coils is

$$\mathbf{B}_i^{\text{ctrl}} = \sum_{j=1}^{N_c} \mathbf{B}_{i,j}^{\text{coil}}. \tag{7}$$

If permanent magnets are also part of the control system, their static fields can be modeled separately and subtracted; the coil contribution remains as above. The formulation is thus hardware-agnostic.

4) Measurement model and field separation: To establish the mapping from measurements to capsule pose while removing external interference, the measured field at sensor i is decomposed as

$$\mathbf{B}_i^{\text{meas}} = \mathbf{B}_i^{\text{cap}} + \mathbf{B}_i^{\text{ctrl}} + \mathbf{B}_i^{\text{bkg}} + \mathbf{n}_i, \tag{8}$$

where $\mathbf{B}_i^{\text{bkg}}$ is a calibrated background field (obtained with zero current) and $\mathbf{n}_i$ denotes measurement noise. After compensation, the capsule-only observation is

$$\bar{\mathbf{B}}_i^{\text{cap}} = \mathbf{B}_i^{\text{meas}} - \mathbf{B}_i^{\text{ctrl}} - \mathbf{B}_i^{\text{bkg}}, \tag{9}$$

With N_m capsules present simultaneously, linear superposition gives

$$\mathbf{B}_i^{\text{cap}} = \sum_{k=1}^{N_m} \mathbf{B}_i^{\text{cap}}(\boldsymbol{\xi}^{(k)}), \tag{10}$$

where $\boldsymbol{\xi}^{(k)}$ is the pose of the k-th capsule. Using the above observations and the dipole model, pose inversion proceeds directly without control, or with prior subtraction of when control is active. This unified framework handles localization of an arbitrary number of capsules.

C. Problem Formulation and Global Optimization-based Inversion

Let the stacked readings from all N_s tri-axial sensors be

$$\mathbf{y} = \left[\bar{\mathbf{B}}_1^{cap\ \mathrm{T}}, \cdots, \bar{\mathbf{B}}_{N_s}^{cap\ \mathrm{T}}\right]^{\mathrm{T}} \in \mathbb{R}^{3N_s}. \tag{11}$$

Let the stacked 5-DoF states of all N_m capsules be X, with dimension $d = 5N_m$:

$$\mathbf{X} = \left[\boldsymbol{\xi}_1^{\mathrm{T}}, \cdots, \boldsymbol{\xi}_{N_m}^{\mathrm{T}}\right]^{\mathrm{T}} \in \mathbb{R}^{5N_m}. \tag{12}$$

The objective of magnetic capsule localization is to infer the capsule state vector X from the measured magnetic field y under bounded constraints. This inverse problem is high-dimensional and multimodal: the decision space is large; the capsule's magnetic magnitude and orientation angles span wide ranges; and measurement noise and compensation errors further complicate the search. To address these challenges, a PMMN-DBO algorithm is developed that performs global optimization via parallel multi-task search, mirrored boundary reflection, elite-solution mutation, and a nonlinear convergence factor. These mechanisms enhance stability and computational efficiency, enabling robust, accurate, real-time localization of capsule robots. Based on the measured magnetic field and the magnetic models in (2), the objective function is formulated as:

$$\min_{\mathbf{X}\in\chi} F(X) = \sum_{i=1}^{N_s} \left\| \sum_{k=1}^{N_m} \hat{\mathbf{B}}_i^{cap}(\boldsymbol{\xi}_k) - \bar{\mathbf{B}}_i^{cap} \right\|_2^2, \tag{13}$$

where the objective $F(\mathbf{X})$ evaluates the quality of a candidate solution; the goal is to minimize the deviation between the

modeled field and the measured field. The feasible set is defined as:

$$\chi = \left\{ \boldsymbol{X} = \left[\boldsymbol{\xi}_1^{\mathrm{T}}, \cdots, \boldsymbol{\xi}_{N_m}^{\mathrm{T}} \right] \mid \boldsymbol{L} \leq \boldsymbol{\xi}_k^{\mathrm{T}} \leq \boldsymbol{U}, \forall k \right\}. \quad (14)$$

where the upper and lower bounds of each dimension are $\mathbf{U} = [U_x, U_y, U_z, \pi, 2\pi]^\top$, $\mathbf{L} = [L_x, L_y, L_z, 0, 0]^\top$.

PMMN-DBO workflow:

1) Initialization: PMMN-DBO launches N_p independent sub-optimization subtasks with population size N_{pop}. Within the feasible region, the n-th individual is randomly initialized as:

$$\mathbf{X}_n^{(0)} = \mathbf{L} + (\mathbf{U} - \mathbf{L}) \odot \mathbf{s}_n, \mathbf{s}_n \sim U(0,1)^d. \quad (15)$$

According to the ratio vector $\boldsymbol{\rho} = [\rho_1, \rho_2, \rho_3, \rho_4]^\top (\rho_q > 0, \sum_{q=1}^4 \rho_q = 1)$, the N_{pop} individuals are divided into four groups (two groups for exploration, two for development), with group sizes $N_q = \lfloor \rho_q N_{pop} \rfloor \, (q = 1, 2, 3), N_4 = N_{pop} - \sum_{q=1}^3 N_q$. In each iteration, groups update their individuals under different strategies.

2) Iterations: After initialization, each subtask runs Nt iterations. Every iteration updates all candidates and computes their objective values, retaining the best for that subtask. Iteration t includes:

a) Update of the nonlinear convergence factor: PMMN-DBO adopts a nonlinear factor R and updates it each iteration:

$$R = \cos^2\left(\frac{\pi t}{2N_t}\right). \quad (16)$$

As iterations proceed, R smoothly decays from 1 to 0; early on, $R \approx 1$ yields larger search steps and stronger global exploration, while later, a small R strengthens local development and promotes convergence stability.

b) Grouped updates: Group 1 uses two update modes and selects one by the rule:

$$\mathbf{X}_n^{(t)} = \begin{cases} \mathbf{X}_{n,\mathrm{I}}^{(t)}, & u_1 \geq p_1 \\ \mathbf{X}_{n,\mathrm{II}}^{(t)}, & u_1 < p_1 \end{cases}, \quad (17)$$

where $\mathbf{X}_n^{(t)}$ is the n-th individual at iteration t, $u_1 \sim U(0,1), p1 \in (0,1)$.

Mode I update:

$$\begin{aligned} \mathbf{X}_{n,\mathrm{I}}^{(t)} = \mathbf{X}_n^{(t-1)} + a_1 \cdot a_2 \odot \mathbf{X}_n^{(t-2)} \\ + a_3 \cdot \left| \mathbf{X}_n^{(t-1)} - \mathbf{X}_W^{(t-1)} \right| \end{aligned}, \quad (18)$$

where $\mathbf{X}_n^{(t-1)}$ and $\mathbf{X}_n^{(t-2)}$ are the n -th individual at iterations $t-1$ and $t-2$, $\mathbf{X}_W^{(t-1)}$ is the global best at $t-1$, $\odot$ is elementwise product, $|\cdot|$ is elementwise absolute value, $a_1, a_3 \in (0,1)$, $a_2 = \mathrm{sign}(u_2 - p_2)$, $u_2 \sim U(0,1)$, $p_2 \in (0,1)$.

Mode II update:

$$\mathbf{X}_{n,\mathrm{II}}^{(t)} = \begin{cases} \mathbf{X}_n^{(t-1)}, & a_4 \in \left\{0, \frac{\pi}{2}, \pi\right\}, \\ \mathbf{X}_n^{(t-1)} + \tan(a_4) \left| \mathbf{X}_n^{(t-1)} - \mathbf{X}_n^{(t-2)} \right|, & \text{otherwise} \end{cases} \quad (19)$$

where $a_4 \sim U(0, \pi)$.

Group 2 updates as:

$$\begin{aligned} \mathbf{X}_n^{(t)} = \mathbf{X}_{\mathrm{LB}} + b_1 \odot \left(\mathbf{X}_n^{(t-1)} - \mathbf{U}_2 \right) \\ + b_2 \odot \left(\mathbf{X}_n^{(t-1)} - \mathbf{L}_2 \right) \end{aligned}, \quad (20)$$

where $\mathbf{X}_{LB}$ is the current local best; $\mathbf{U}_2 = \min\{(1+R)\mathbf{X}_{LB}, \mathbf{U}\}$, $\mathbf{L}_2 = \max\{(1-R)\mathbf{X}_{LB}, \mathbf{L}\}$ are Group-2 search bounds; $\min\{\cdot,\cdot\}$ and $\max\{\cdot,\cdot\}$ are elementwise; $\mathbf{b}_1, \mathbf{b}_2 \sim U(0,1)^d$.

Group 3 updates as:

$$\begin{aligned} \mathbf{X}_n^{(t)} = \mathbf{X}_n^{(t-1)} + c_1 \odot \left(\mathbf{X}_n^{(t-1)} - \mathbf{U}_3 \right) \\ + c_2 \odot \left(\mathbf{X}_n^{(t-1)} - \mathbf{L}_3 \right) \end{aligned}, \quad (21)$$

where $\mathbf{U}_3 = \min\{(1+R)\mathbf{X}_B^{(t-1)}, \mathbf{U}\}$, $\mathbf{L}_3 = \max\{(1-R)\mathbf{X}_B^{(t-1)}, \mathbf{L}\}$ are Group-3 bounds, $\mathbf{c}_1, \mathbf{c}_2 \sim N(0,1)^d$, and $\mathbf{X}_B^{(t-1)}$ is the global best at iteration $t-1$.

Group 4 updates as:

$$\begin{aligned} \mathbf{X}_n^{(t)} = \mathbf{X}_n^{(t-1)} + d_1 \cdot d_2 \odot \left(\left| \mathbf{X}_n^{(t-1)} - \mathbf{X}_{\mathrm{LB}} \right| \right. \\ \left. + \left| \mathbf{X}_n^{(t-1)} - \mathbf{X}_B^{(t-1)} \right| \right) \end{aligned}, \quad (22)$$

where $d_1 \in (0,1]$, $d_2 \sim N(0,1)^d$.

c) Boundary reflection: PMMN-DBO introduces mirrored boundary handling, reprojecting any out-of-bounds individual as:

$$\mathbf{X}_{n,new}^{(t)} = \mathbf{L} + \mathbf{U} - \mathbf{X}_n^{(t)} + |\mathbf{L} - \mathbf{X}_n^{(t)}| - |\mathbf{X}_n^{(t)} - \mathbf{U}|. \quad (23)$$

This effectively processes boundary crossings, enabling efficient global exploration near the borders while avoiding simple truncation that causes step loss and getting stuck on the boundary.

d) Elite mutation: To enhance local development and prevent premature convergence, PMMN-DBO introduces elite mutation. At the end of iteration t, take the current global best XB(t) and randomly choose two individuals to generate Nmut mutation candidates. The i-th candidate is:

$$\mathbf{X}_{B,m} = \mathbf{X}_B^{(t)} + \boldsymbol{\nu}_1 \odot (\mathbf{X}_{w_1}^{(t)} - \mathbf{X}_B^{(t)}) + \boldsymbol{\nu}_2 \odot (\mathbf{X}_{w_2}^{(t)} - \mathbf{X}_B^{(t)}), \quad (24)$$

where $\boldsymbol{\nu}_1, \boldsymbol{\nu}_2 \sim \chi^2(R)$, $w_1, w_2 \in \{1, 2, ..., N_{pop}\}$, $w_1 \neq w_2$; new individuals use boundary reflection to remain valid. As iterations proceed, R decays and mutation amplitude shrinks adaptively: early stages promote exploration and jumps from local optima; later stages strengthen local convergence for refined search. Among all mutation candidates and the current best, greedy selection retains the one with the lower objective as the new global best, which is then broadcast to the subtask.

e) Final solution selection: Each of the Np parallel subtasks returns its candidate set $\{\mathbf{X}_p\}_{p=1}^{N_p}$ and corresponding objectives $\{F(\mathbf{X}_p)\}_{p=1}^{N_p}$. The final solution is chosen as the best among them:

$$\mathbf{X} = \underset{p \in [1,2,\ldots,N_p]}{\arg\min} \; F(\mathbf{X}_p). \quad (25)$$

Figure 3 illustrates the workflow of the PMMN-DBO algorithm. In summary, driven by the objective function, PMMN-DBO stably converges to high-quality solutions within a limited number of iterations, while maintaining a good balance of accuracy and efficiency in multi-agent, high-dimensional, and strongly constrained settings. Moreover, many hyperparameters are task-adjustable—such as the number of parallel subtasks N_p, total iterations N_t, group ratios $\boldsymbol{\rho}$, number of mutations N_v, the schedule of the convergence factor R, and the update coefficients of each group. These can be tuned according to the specific application and computational budget to meet different requirements for accuracy, speed, and robustness.

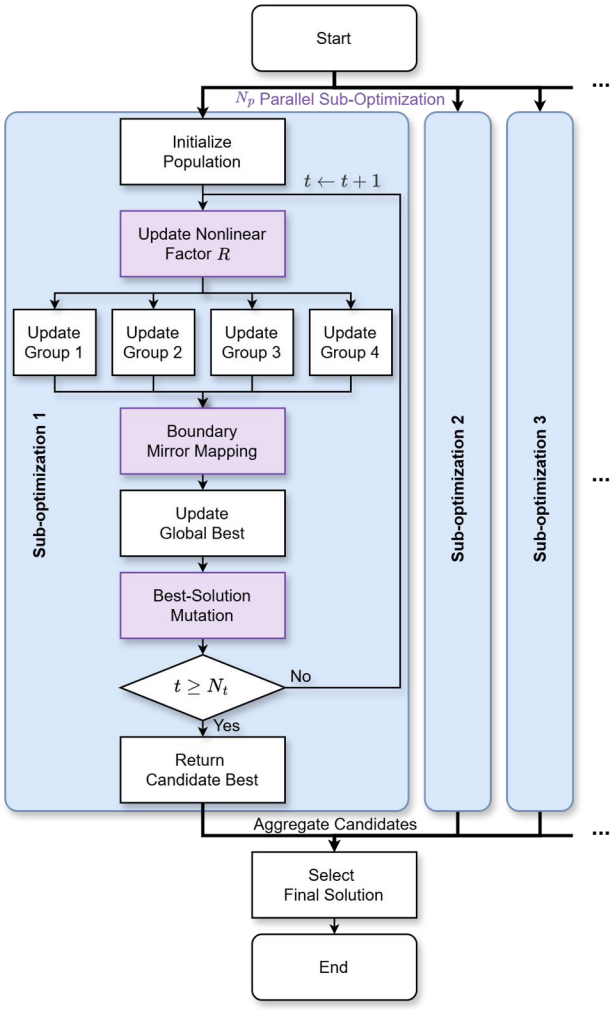

Fig. 3. Flowchart of the PMMN-DBO algorithm.

III. EXPERIMENTS AND RESULTS

A. Experimental Setup

All computations were performed on a Windows 11 Pro workstation running MATLAB R2025a, equipped with an Intel Core i9-13900H processor. Magnetic-field simulations were conducted in COMSOL Multiphysics 6.3. To meet the open-access workspace requirements of clinical capsule-robot applications, a 4×4 planar sensor-array layout was adopted. Each sensing unit is a tri-axial AMR sensor (Memsic MMC5603NJ). All sensors communicate through two TI TCA9548A I2C multiplexers for bus expansion and routing. The center-to-center spacing between adjacent sensors in the array is 30 mm.

System control and data transfer are provided by an ST NUCLEO-U575ZI controller. Raw data are uploaded to a host computer for real-time logging and processing under a unified protocol, as illustrated in Fig. 4. Prior to formal experiments, hard-iron and soft-iron calibration, as well as background-field calibration at the installed positions, were completed to ensure localization accuracy.

The capsule's internal magnet is a cylindrical N52 Nd–Fe–B magnet with a diameter of 10 mm and a height of 5 mm. For convenience, the capsule shell was removed in some tests, exposing only the magnet.

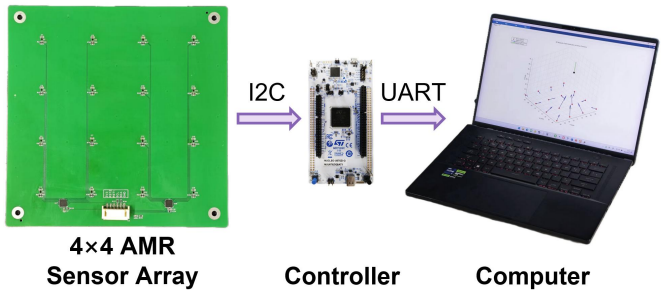

Fig. 4. Hardware and data flow of the magnetic localization system.

B. Single-capsule Localization

To evaluate localization performance for a single capsule, the capsule was placed at a representative workspace pose satisfying observability, and magnetic data were collected using the sensor array. 100 independent runs with random initialization, position error, angular error, and per-solve computation time were recorded (see Fig. 5). Parameters: $N_p = 3$, $N_t = 125$, $N_v = 10$, $\rho = [5, 9, 7, 14]^\top$.

Figure 5(a) shows a localization error of 0.59 ± 0.30 mm; Fig. 5(b) reports an angular error of 0.69 ± 0.37°; Fig. 5(c) indicates an average per-solve time of 0.0202 ± 0.0036 s, with no significant error spikes caused by trapping in local optima. Overall, in the single-capsule scenario, the localization framework achieves high accuracy and stability within a short computation time.

A performance comparison of different optimization algorithms was conducted. DBO serves as the baseline version of PMMN-DBO with all improvements removed, and its parameter settings are kept identical to those of PMMN-DBO. PSO, GA, and SA are implemented using MATLAB's built-in functions, each with 1000 iterations; further increasing the iterations yields limited performance gains.

As shown in Fig. 6, PMMN-DBO achieves significantly higher position and angular accuracy than the competing algorithms while maintaining good real-time performance.

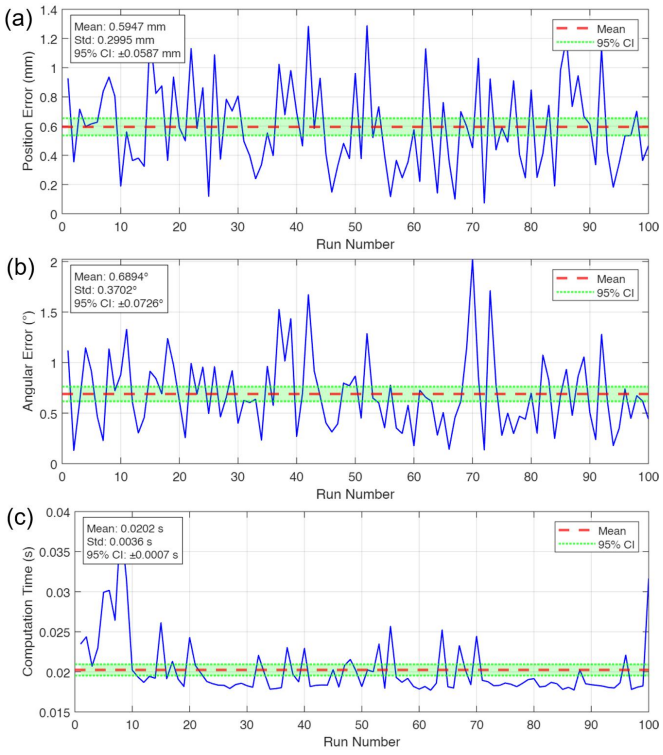

Fig. 5. Performance evaluation of the PMMN-DBO algorithm for single-capsule localization. (a) Position error, (b) Angular error, and (c) Computation time over 100 independent runs.

For 100 independent runs under the same capsule robot pose, DBO and PSO exhibit shorter average runtimes but notably degraded accuracy. Specifically: DBO: 14.48±17.94 mm, 24.29±38.58°, 0.0085±0.0010 s; PSO: 24.66±11.01 mm, 37.77±19.64°, 0.0062±0.0015 s. Compared with PMMN-DBO, DBO shows a similar median but a longer right tail in the error distribution, with a few large errors—indicative of getting trapped in local optima—leading to higher overall variability. The improvements in PMMN-DBO increase computational overhead and thus runtime. GA and SA are inferior in both accuracy and efficiency and also show larger variability: GA: 25.77±11.7 mm, 40.97±22.13°, 0.0201±0.0029 s; SA: 29.99±14.16 mm, 45.53±24.94°, 0.0367±0.0021 s.

In summary, PMMN-DBO offers the best balance between accuracy and efficiency, demonstrating stronger global search and convergence control capabilities and effectively reducing instability caused by local optima and noise perturbations.

C. Multi-capsule Localization

The scalability of the algorithm was validated in multi-magnet scenarios. Experiments used a fixed plate with equally spaced holes, placing $N_m \in \{1, 2, 3\}$ capsule magnets at known positions. For each N_m, the optimizer was randomly initialized, repeatedly executed, and the localization errors and computation times of each magnet were recorded. Figures 7(b)–(d) report the position error, angular error, and per-run computation time versus N_m, with bars indicating means.

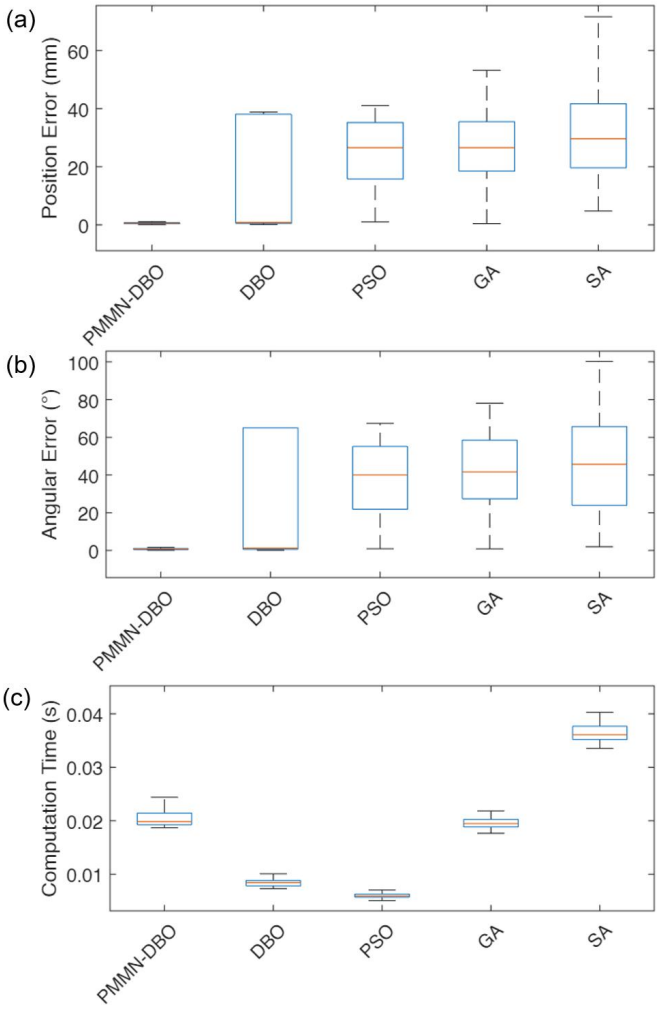

Fig. 6. Performance comparison of different optimization algorithms for magnetic localization. Based on 100 runs, box plots show the statistical distributions of (a) position error, (b) angular error, and (c) per-solve computation time.

As N_m increases, the problem dimensionality and nonlinearity grow, leading to a marked rise in overall complexity; using single-magnet default hyperparameters degrades convergence and accuracy. A parameter-adaptive scheme with relaxed iteration caps was therefore adopted: 500 iterations for $N_m = 2$ and 2000 for $N_m = 3$, while scaling the population size and the number of subtasks linearly with the product of magnet count and parameter dimension to maintain stable convergence.

For $N_m = 2$, the mean position/angular errors are 1.28 mm/1.13°, with a computation time of 0.8381±0.0311 s; the error increases slightly but remains acceptable. For $N_m = 3$, the mean position/angular errors are 2.56 mm/2.83°, with a computation time of 7.86±0.14 s, indicating larger errors and variance; nevertheless, with the above scaling, the method still converges stably to consistent solutions. Computation time grows with N_m, consistent with the expected near-linear increase in variable count.

In summary, as the number of magnets increases,

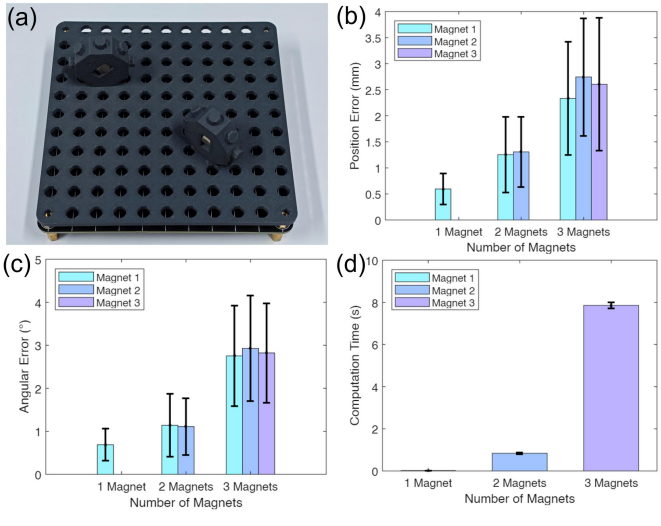

Fig. 7. Localization experiments with multiple capsule robots. (a) Magnet fixture plate and multi-magnet arrangement; (b) Position error versus the number of magnets N_m; (c) Angular error and standard deviation versus the number of magnets Nm; (d) Computation time per run versus the number of magnets N_m.

the proposed localization framework achieves robust, high-accuracy localization, while maintaining good convergence stability and scalability in multi-capsule settings. Hyperparameters can be adaptively tuned to the target accuracy and computational budget to meet different application requirements.

D. Synchronized Control and Localization

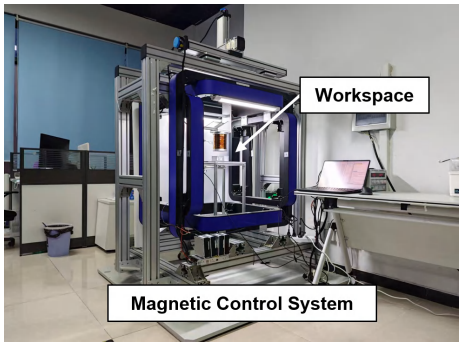

Fig. 8. External magnetic control system for capsule robot.

Synchronized Control and Localization experiment was conducted on an external magnetic control system capable of levitation coupled 5-DoF pose regulation. The system comprises seven coils, six fixed and one position-adjustable. The transformations from each coil's local frame to the world frame were obtained by calibration. Closed-loop magnetic force (upward) and stabilizing torque are generated using the system's onboard sensors to achieve levitation and orientation control. The sensor array is mounted beneath the container and kept sufficiently far from the capsule to satisfy far-field conditions.

To assess synchronized control-localization, the controller and the localization module run in parallel. The controller

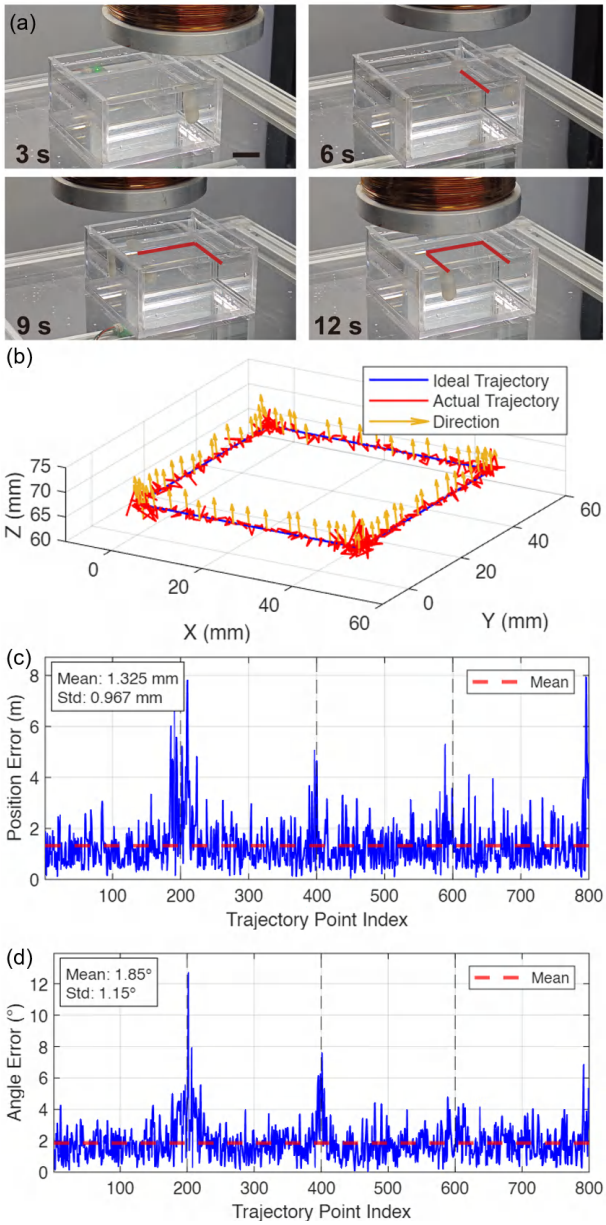

Fig. 9. Synchronized control–localization experiment. (a) Under the external magnetic control system, the capsule is fully suspended in a liquid with a stable pitch angle and follows a rectangular path (side length: 50 mm; pitch angle: 11°). (b) Comparison between the 3D nominal trajectory and the actual trajectory. (c) Position error versus time (trajectory point index). (d) Angular error versus time.

performs closed-loop tracking of a predefined spatial rectangular trajectory by itself, without using the localization estimates reported in this work for feedback. The localization system is only used to estimate and log the capsule's pose in real time. Fig. 9(a) shows levitated closed-loop motion along the rectangular path in liquid; Fig. 9(b) compares the 3D desired trajectory with the trajectory reconstructed by localization; Fig. 9(c)–(d) plot the position and angular errors versus time (trajectory point index), respectively.

The errors mainly stem from measurement noise and discrepancies between the actual coils and their models;

additionally, results indicate smaller errors along the four edges of the rectangle and the expected spikes at the corners. These transients arise when the capsule changes direction and speed at corner points, causing brief jitter that reflects the coupling between trajectory changes, control, and localization. The statistics are: position error 1.33±0.97 mm and angular error 1.85±1.15°. With a conservative real-time localization rate of 20 Hz, the proposed method demonstrates real-time performance and stability under dynamic control.

IV. CONCLUSIONS

This work proposes and systematically validates a unified magnetic 5-DoF localization framework for capsule robots, establishing an end-to-end pipeline that integrates layered multi-source magnetic field modeling, online external-field compensation, and global inversion. The framework achieves algorithm–hardware co-design and real-time operation across single-capsule, multi-capsule, and synchronized control–localization scenarios. At its core, PMMN-DBO is proposed, which incorporates parallel multi-task optimization, mirrored boundary reflection, elite-solution mutation, and a nonlinear convergence factor, yielding a unified balance of real-time performance, high accuracy, and robustness.

Experimental results show that, for a single capsule, the method converges reliably over 100 independent runs with position/angular errors of approximately 0.59 mm/0.69° and a per-run time of 0.0202 s. Compared with DBO, PSO, GA, and SA, it attains superior accuracy–stability–efficiency trade-offs on nonconvex, multimodal objectives. In multi-capsule settings, errors remain controlled with stable convergence as the number of magnets increases, and runtime scales near-linearly with problem size; the mean errors are 1.28 mm/1.13° for two capsules and 2.56 mm/2.83° for three capsules. In synchronized control–localization, with a conservative 20 Hz localization rate, the mean errors are 1.33 mm/1.85°, confirming the feasibility and robustness of parallel control–localization.

Future work will focus on fusing multimodal sensing to reconstruct full 6-DoF pose (including roll), and on introducing temporal priors and filtering/smoothing that leverage dynamics and control inputs, further supporting clinical-grade closed-loop magnetic control.

In summary, the proposed unified magnetic 5-DoF localization framework achieves stable, accurate, and real-time capsule localization in complex external fields and open environments, providing a reusable algorithm–system foundation for clinical-grade closed-loop magnetic control, including precise navigation, targeted delivery, and minimally invasive interventions.

REFERENCES

[1] Z. Liao et al., "Accuracy of Magnetically Controlled Capsule Endoscopy, Compared With Conventional Gastroscopy, in Detection of Gastric Diseases," Clinical Gastroenterology and Hepatology, vol. 14, no. 9, pp. 1266–1273.e1, Sep. 2016.

[2] A. Wang et al., "Wireless capsule endoscopy," Gastrointestinal Endoscopy, vol. 78, no. 6, pp. 805–815, Dec. 2013.

[3] Y. Sun et al., "Magnetically driven capsules with multimodal response and multifunctionality for biomedical applications," Nat Commun, vol. 15, no. 1, p. 1839, Feb. 2024.

[4] L. Song et al., "The Design of 3-D Space Electromagnetic Control System for High-Precision and Fast-Response Control of Capsule Robot with 5-DOF," in 2019 International Conference on Intelligent Robotics and Applications, pp. 202–212, Jan. 2019.

[5] L. Song et al., "Motion Control of Capsule Robot Based on Adaptive Magnetic Levitation Using Electromagnetic Coil," IEEE Transactions on Automation Science and Engineering, vol. 20, no. 4, pp. 2720–2731, Oct. 2023.

[6] H. Zhou, C. C. Mayorga-Martinez, S. Pané, L. Zhang, and M. Pumera, "Magnetically Driven Micro and Nanorobots," Chem. Rev., vol. 121, no. 8, pp. 4999–5041, Apr. 2021.

[7] P. E. Dupont et al., "A decade retrospective of medical robotics research from 2010 to 2020," Science Robotics, vol. 6, no. 60, p. eabi8017, Nov. 2021.

[8] Z. Zeng, F. Wang, J. Zhao, C. Wang, C. Li, and L. Feng, "The Control System for 5-DOF Magnetic Levitation Capsule Robot," in 2023 WRC Symposium on Advanced Robotics and Automation (WRC SARA), Aug. 2023, pp. 174–179.

[9] K. M. Popek, T. Schmid, and J. J. Abbott, "Six-Degree-of-Freedom Localization of an Untethered Magnetic Capsule Using a Single Rotating Magnetic Dipole," IEEE Robotics and Automation Letters, vol. 2, no. 1, pp. 305–312, Jan. 2017.

[10] E. Paperno and A. Plotkin, "Cylindrical induction coil to accurately imitate the ideal magnetic dipole," Sensors and Actuators A: Physical, vol. 112, no. 2–3, pp. 248–252, May 2004.

[11] S. Song, C. Hu, and M. Q.-H. Meng, "Multiple Objects Positioning and Identification Method Based on Magnetic Localization System," IEEE Transactions on Magnetics, vol. 52, no. 10, pp. 1–4, Oct. 2016.

[12] C. Hu, M. Q. Meng, and M. Mandal, "Efficient magnetic localization and orientation technique for capsule endoscopy," in 2005 IEEE/RSJ International Conference on Intelligent Robots and Systems, Aug. 2005, pp. 628–633.

[13] C. Hu, W. Yang, D. Chen, M. Q.-H. Meng, and H. Dai, "An improved magnetic localization and orientation algorithm for wireless capsule endoscope," in 2008 30th Annual International Conference of the IEEE Engineering in Medicine and Biology Society, Aug. 2008, pp. 2055–2058.

[14] W. Yang, C. Hu, M. Q.-H. Meng, S. Song, and H. Dai, "A Six-Dimensional Magnetic Localization Algorithm for a Rectangular Magnet Objective Based on a Particle Swarm Optimizer," IEEE Transactions on Magnetics, vol. 45, no. 8, pp. 3092–3099, Aug. 2009.

[15] S. Su et al., "Investigation of the Relationship Between Tracking Accuracy and Tracking Distance of a Novel Magnetic Tracking System," IEEE Sensors Journal, vol. 17, no. 15, pp. 4928–4937, Aug. 2017.

[16] Z. Teng, J. Ren, H. Sun, Q. Liu, J. Liu, and Q. Wang, "Study on Real-Time Tracking of Wireless Capsule Endoscope Based on LM-EM Algorithm," IEEE Transactions on Instrumentation and Measurement, vol. 74, pp. 1–10, 2025.

[17] J. Yang, J. Wei, F. Wang, L. Song, J. Zhao, and L. Feng, "A Localization Method for the Magnetic Levitation Capsule Robot," in 2022 WRC Symposium on Advanced Robotics and Automation (WRC SARA), Beijing, China: IEEE, Aug. 2022, pp. 152–159.

[18] Z. Zeng, F. Wang, C. Li, M. Tan, S. Wang, and L. Feng, "Dung Beetle Optimizer-based High-precision Localization for Magnetic-Controlled Capsule Robot," in 2024 IEEE/RSJ International Conference on Intelligent Robots and Systems (IROS), Oct. 2024, pp. 2347–2352.

[19] J. Xue and B. Shen, "Dung beetle optimizer: a new meta-heuristic algorithm for global optimization," J Supercomput, vol. 79, no. 7, pp. 7305–7336, May 2023.

[20] S. Song, C. Hu, and M. Q.-H. Meng, "Multiple Objects Positioning and Identification Method Based on Magnetic Localization System," IEEE Transactions on Magnetics, vol. 52, no. 10, pp. 1–4, Oct. 2016.